

Anonymous

Tactile sensory organs for sensing 3D force, such as human skin and fish lateral lines, are indispensable for organisms. With their sensory properties enhanced by layered structures, typical sensory organs can achieve excellent perception as well as protection under frequent mechanical contact. Here, inspired by these layered structures, a split-type magnetic soft tactile sensor with wireless 3D force sensing and a high accuracy (1.33%) fabricated by developing a centripetal magnetization arrangement and theoretical decoupling model is introduced. The 3D force decoupling capability enables it to achieve a perception close to that of human skin in multiple dimensions without complex calibration. Benefiting from the 3D force decoupling capability and split design with a long effective distance (>20 mm), several sensors are assembled in air and water to achieve delicate robotic operation and water flow-based navigation with an offset $<1.03\%$, illustrating the extensive potential of magnetic tactile sensors in flexible electronics, human-machine interactions, and bionic robots.

1. Introduction

Organismic evolution has resulted in a wide range of functional sensory organs, which enable creatures to perceive their surrounding environment and prey to increase their survivability. One of the most interesting perceptions is the tactile sense

for 3D mechanical force, enabling humans and other animals to perform delicate operations and become effective predators. With continuous advancements in algorithms, materials, and fabrication techniques, a wide variety of tactile sensors have been developed through the biomimetic engineering of biological sensory organs, such as the lateral line of fish^[1–3] and human skin,^[4–7] to make machines more interactive, adaptive and more intelligent.^[8–10] For example, tactile sensors can sense the movements of the human wrist to control robotic arms to make corresponding actions,^[9] and they can be used as skin receptors for health monitoring^[11,12] and artificial prosthetics.^[13,14] Another example is bionic lateral lines for fluid force measurement, which can be used for the force compensation and position tracking of autonomous underwater vehicles.^[1] Currently, devel-

oped tactile sensors are based on a variety of principles, including piezoelectric,^[15–17] piezoresistive,^[18–21] capacitive,^[22–25] optical,^[26–28] and triboelectric^[29–31] principles. Other studies have combined several tactile sensors with different properties according to their respective principles, e.g., imitating human skin with different mechanoreceptors, to sense various forms of contact and force.^[32–34] Most of these studies have made great progress in high-precision perception and high-speed response. With the development of tactile sensor performance, however, the complexity of internal circuits is increasing, which results in very difficult and complicated circuit fabrication. Moreover, the operational stability of tactile sensors with such internal circuits is difficult to guarantee during frequent mechanical contact due to the high damage risk of the circuits, which do not have the same regenerative functions as naturally evolved skin nerve endings. In addition, the lack of perceptual dimension also makes it difficult for existing sensors to match the perception ability of human skin. Consequently, in-depth developments have put forwards new challenges for tactile sensors, such as achieving a high stability, fast fabrication and multiple perceptual dimensions, and have led to further conceptualization and research on the design, fabrication, and, more importantly, principle of tactile sensors.

Recently, magnetic-based tactile sensors have received extensive attention due to their simple structure, high physical robustness, low cost, and wireless penetrability.^[35–37] The development of magnetic tactile sensors can be applied in many applications such as robot precision grasping, texture characterization,

flow velocity measurement, and medical treatment.^[38–41] However, embedding hard permanent magnets weakens the flexibility of the sensor, making it susceptible to damage under large external shocks. The application of flexible magnetic materials further improves the flexibility of the sensor^[42,43] and, more importantly, enables designable magnetization^[44,45] and provides more possibilities for magnetic-based tactile sensors. For example, a magnetic-based soft tactile sensor amazingly realized the self-decoupling of normal force and shear force perception with the most basic sandwich structure, which was attributed to a brilliantly designed flexible magnetic film with a 1D sinusoidal magnetization profile.^[46] Moreover, combined with machine learning technology, it enabled high-quality superresolution tactile sensing on every cell in an array. However, even though considerable breakthroughs have been made in research on magnetic-based tactile sensors, there are still many challenges to overcome, such as the inability to decouple the perception of 3D forces and the limitation of the short working distance of sensors to magnetic components. A sensor with traditional polynomial fitting is reported, which uses multiple magnetic pixels, and operates on the gradient of the magnetic field to make the magnetic sensors immune to stray magnetic fields up to 2 mT.^[47] However, it keeps a small distance between the Hall sensor and the magnetic component, which limits the advantages of the wireless penetrability. In addition, most of the existing magnetic-based tactile sensors have an embedded Hall sensor in their flexible layer, which not only reduces flexibility but also does not allow the advantage of wireless penetrability to be fully utilized. (See Table S2, Supporting Information, for more details.)

To tackle the above challenges and fully exploit the advantages of magnetic-based tactile sensors, here, we report a magnetic soft tactile sensor with a 3D force-decoupling perception and split-type design that has an accuracy of 2.33% in the normal direction and 1.33% in the shear direction. Mimicking the special layered structure of human skin and fish lateral lines, our tactile sensor is composed of a “touch layer” (a centripetally magnetized flexible magnetic film), “buffer layer” (a silicone elastomer), and “transmission layer” (a Hall sensor). Through the derivation of theoretical model, the centrosymmetric centripetally magnetized magnetic film can realize 3D force decoupling within the working range. Due to the self-decoupling ability, laborious calibration experiments are evitable before utilization of the sensor. Besides, centripetal magnetization also enables an elongation of the working distance between magnetic film and Hall sensor, thereby ensuring the split-design of the tactile sensor by separating the “transmission layer” from the “touch layer” and the “buffer layer,” thus taking full advantage of the wireless penetrability. In this way, we can easily replace the “buffer layer” to adapt to different application scenarios. Equipped with our magnetic tactile sensor, a robotic hand can stably grasp objects of varying mass and simultaneously adapt to large external disturbances, similar to a human hand. In addition, the decoupling of 3D force perception enables our sensor to act as a “joystick” to control the movements of a tracked robot, illustrating extensive potential in human–machine interactions. Furthermore, with the ability of 3D decoupling, once the Hall sensor is assembled in the working region below magnetic film, the axial offset during assembly will not affect the perception performance. After replacing the “buffer layer” with a grid-shaped substrate specialized for shear sensing,

we can install the sensor separately on the inner and outer sides of a ship’s hull, where our magnetic tactile sensor can sense the sailing speed of the ship in the water, similar to the lateral line of fish, while keeping the hull intact and without any perforations.

2. Results and Discussion

2.1. Design and Performance of the Magnetic Tactile Sensor

By mimicking the layered structure of sensitive mechanoreceptors, such as human skin (especially for normal force) and fish lateral lines (especially for shear force), we design and fabricate a magnetic soft tactile sensor with a sandwich-like structure. **Figure 1a** shows the basic structure of this sensor and the composition of each layer. The “touch layer” is a flexible magnetic film (20 mm × 20 mm; thickness, 1 mm) made by mixing the elastomer matrix and NdFeB micromagnets. The composition of the magnetic film under the micro-CT scan is shown in **Figure 1b**, where the gray part is the elastomer matrix, and the blue particles are NdFeB micromagnets. The magnetization direction of the magnetic film is from the four sides to the center, which is achieved by folding the square magnetic film into the shape of an arrowhead and placing it vertically in a strong magnetic field (4 T) to magnetize (Text S6 and S7, Supporting Information). The “buffer layer” is a flexible layer made of soft silicone elastomer (Ecoflex 00-30; thickness 10 mm). By mixing silicone oil (PMX-200; viscosity 5 cs) into it, we can change the elastic modulus of this layer, thereby adjusting the measurement range and sensitivity of the sensor to force. The “transmission layer” is a printed circuit board (PCB; thickness 1 mm) with a mounted 3D Hall sensor (MLX90393), which can measure the magnetic flux density along three axes. Moreover, as shown in the physical photo of the tactile sensor in the lower middle of **Figure 1a**, by taking the spacer plate as the dividing line, the “touch layer” and “buffer layer” can be installed separately from the “transmission layer” to meet the necessary wireless working requirements. (The distance between the magnetic film and the Hall sensor in the photo is 20 mm.) When an external force is applied to the “touch layer” of the sensor, the magnetic field lines of the magnetic film are displaced due to structural deformation, and then the fixed Hall sensor senses the displacement of the magnetic film by detecting the change in the three-axis magnetic signal. Furthermore, according to the corresponding relationship between the force and displacement in the “buffer layer,” the perception of the external 3D force is finally realized.

The self-decoupling formulas of the magnetic film are derived from an ideal magnetic film with an infinite period sinusoidal magnetization profile (Text S1, Supporting Information). Because infinite period plane and its magnetization is impossible to achieve in experiment. We used the folding method with similar magnetization (limited periods, $n \times n$) to replace it. As shown in **Figure 1c,d**, the comparison of the magnetic field distribution (along the X-axis, $y = 0$ and $z = -20$ mm) below the magnetic film between ideal and folding magnetization (5×5 periods) is presented. After the linear correction of B_z ($B_z' = kB_z + c$, $k = 1.09$, $c = 156.16$) only, the triaxial magnetic field can agree well with the ideal distribution, which proves the feasibility of using folding magnetization to approximate ideal magnetization. This conclusion is also applicable for a smaller n in a certain

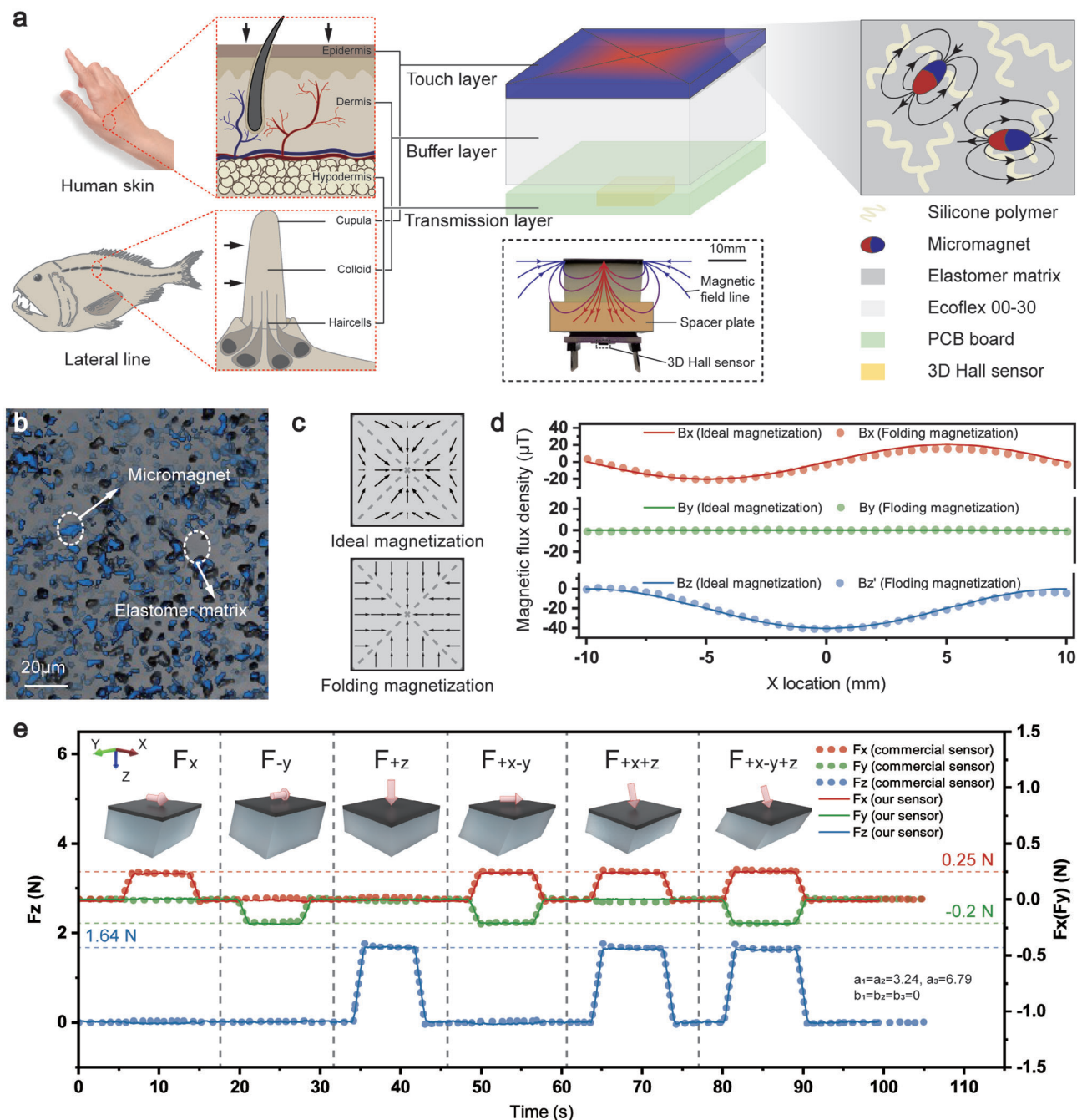


Figure 1. Design and performances of split-type magnetic soft tactile sensor. a) Illustration of the structures of human skin, the lateral line of fish, and the magnetic soft tactile sensor. b) Micro-CT photograph of the magnetic film composed of micromagnets and elastomer matrix. c) The two magnetization modes of the magnetic film. d) The 3D magnetic field distribution comparison below the film along the X-axis ($y = 0, z = -20 \text{ mm}$). e) The demonstration of the 3D force decoupling function of the magnetic soft tactile sensor. (The comparison of the perceiving effect for 3D forces between the commercial sensor and our sensor.)

working range. Therefore, in this work ($z: 0\text{--}3 \text{ mm}$, $y: -3 \text{ to } 3 \text{ mm}$, $x: -3 \text{ to } 3 \text{ mm}$), we selected the 1×1 period folding magnetic film with smaller size for the characterization and demonstration of our sensors (Text S2, Supporting Information).

Parameters S_z , R_x , and R_y , which are defined in Equation (1), are introduced for 3D decoupling. When various forces in different directions are applied to the “touch layer” of the

sensor, the output exhibits corresponding decoupling signals. When the magnetic film only produces normal displacement along the z -direction (only the force along the z -direction is applied), the signal S_z changes, but the signals R_y and R_x remain constant. When the magnetic film only produces shear displacement along the y -direction (only the force along the y -direction is applied), the signal R_y changes, but the signals S_z and R_x remain

constant. When the magnetic film only produces shear displacement along the x direction (only the force along the x -direction is applied), the signal R_x changes, but the signals S_z and R_y remain constant. In other words, the signal S_z is independently related to the displacement along the z -direction, while R_x and R_y are independently related to the displacements along the x - and y -directions, respectively, indicating that S_z , R_y , and R_x are decoupled from each other within the calibration range (z : 0–3 mm, y : –3 to 3 mm, x : –3 to 3 mm). According to the measurement data, the sensor has an accuracy of 2.33% in the normal direction and 1.33% in the shear direction. Here, S_z , R_x , and R_y are defined as

$$\begin{bmatrix} R_x \\ R_y \\ S_z \end{bmatrix} = \begin{bmatrix} \arctan\left(\frac{B_x}{B_z' - \frac{(B_y'^2 - B_z'^2)}{2B_z'}}\right) \\ \arctan\left(\frac{B_y}{B_z'' - \frac{(B_x'^2 - B_z'^2)}{2B_z''}}\right) \\ \ln\left(\sqrt{\left(B_z'' - \frac{(B_x'^2 - B_z'^2)}{2B_z''}\right)^2 + B_y'^2}\right) \end{bmatrix} \quad (1)$$

where $B_z' = k_1 B_z + c_1$ and $B_z'' = k_2 B_z + c_2$. B_x , B_y , and B_z are the magnetic flux densities along the x -, y -, and z -directions, respectively. k_1 , c_1 and k_2 , c_2 are the compensation coefficients of B_z in R_x , R_y , and S_z , respectively (see Text S3–S5, Supporting Information, for detailed information).

According to these three decoupling parameters and the corresponding relationship between the force and displacement (Text S8, Supporting Information) of the elastomer, our sensor can be used for the decoupling sensing of 3D forces. A rigid commercial six-axis F/T load cell (SRI, M3816B1) is used to verify the force decoupling sensing capability of our sensor, as shown in Figure 1e. Our sensor is fixed on the commercial load cell, applied forces by a 3D mobile platform (PMS-3, Powerscin, Shanghai). The magnetic film is fixed to the platform by a 3D-printed groove. The detailed device and magnetic field raw data can be seen in Text S9 (Supporting Information). We compare the measured value of the 3D hybrid force measured by our sensor and the commercial load cell at 86 s in Figure 1e. The deviations are 0.0069 N (F_x), 0.0026 N (F_y), and 0.016 N (F_z), respectively, and the percentage deviations are 2.76%, 1.32%, and 0.99%, respectively, which also include the unavoidable error brought by the installation. Therefore, we can say that our sensor has the decoupling capability and sensing accuracy comparable to that of the commercial load cell. Meanwhile, unlike the commercial load cell, we only use one sensing unit. It should be clarified that the strength of the geomagnetic field is about 50–60 μ T, which is not negligible compared to the magnetic field strength of the magnetic film. Therefore, after fixing the sensor, we measured and recorded the geomagnetic field first, and then placed the magnetic film to carry out the experiment. When the result was output, by subtracting the recorded geomagnetic field, only the magnetic field strength of the film was obtained. Besides, the signal of the sensor has been filtered due to the obvious vibration when applying force with a mobile platform.

The accurate response of our sensor to external forces of different frequencies and its consistent perceived signals under about 1200 cycles of repeated normal and shear forces show that it has

excellent stability, repeatability and durability. See Text S10 (Supporting Information) for details.

2.2. Force Decoupling Mechanism and Calibration of “Transmission Layer”

The magnetic distribution under the magnetic film is analyzed through mathematical calculations to study the decoupling of the centripetally magnetized film in the y – z plane. According to the molecular circulation hypothesis, we equivalently convert the unidirectional magnetic field in the magnetic film into some current loops in the same direction, and the currents along the z -direction cancel each other out. Finally, the magnetic field of the centripetally magnetized film is equal to the concentric current loops evenly distributed on the upper and lower surfaces of the film (Figure 2a). In this case, the magnetic field distribution of the magnetic film can be calculated by the Biot–Savart law, which states that at any point P, the magnetic field \vec{B} due to an element $d\vec{l}$ of a current is given by

$$\vec{B} = \int \frac{\mu_0 I}{4\pi} \frac{d\vec{l} \times \vec{r}}{r^3} \quad (2)$$

where the constant μ_0 is the permeability of a vacuum and is exactly $4\pi \times 10^{-7}$ T m A^{–1}, I is the current intensity, $d\vec{l}$ is an infinitesimal segment in the same direction as the current, and \vec{r} is a vector that points from $d\vec{l}$ to point P. The detailed calculation process of the magnetic field distribution model is included in Text S3 (Supporting Information). Since the magnetic film is magnetized by the folding method, the crease of the film produces a certain error. Therefore, the parameter J (equivalent current density on the surface of the magnetic film, 1.76×10^5 A m^{–1}) is corrected accordingly. Figure 2b shows the experimental measurements and modified model theoretical calculations of the magnetic distribution in the y – z plane below the magnetic film. With the maximum root-mean-square error (RMSE) between them being only 3.86 μ T (B_z) and 2.13 μ T (B_y), it is verified that the modified model can accurately reflect the real magnetic distribution of the centripetally magnetized film.

Based on the distribution model for magnetic field, we decouple in 3D space and obtain three decoupling parameters S_z , R_y , and R_z , which are expressed in Equation (1). The distribution of decoupling parameter values in the 3D space below the magnetic film can be represented as shown in Figure 2c, where S_z , R_y , and R_x remain constant along their iso-surfaces. For isotropic materials, normal stress and shear stress are independent of each other, so the displacement in each direction can be directly linked to the force. Therefore, the relationships between the decoupling parameters and the external force can be directly obtained from their relationships with the three-axis displacements, which is more convenient to conduct and present. The parameter ΔR_x increases when Δx increases (force in x -direction increases) but remains constant as Δy or Δz increases (force in y - or z -direction increases) (Figure 2d), which further illustrates that the measurement of force in x -direction is independent of the force in y - or z -direction. Similarly, a consistent conclusion can be drawn for

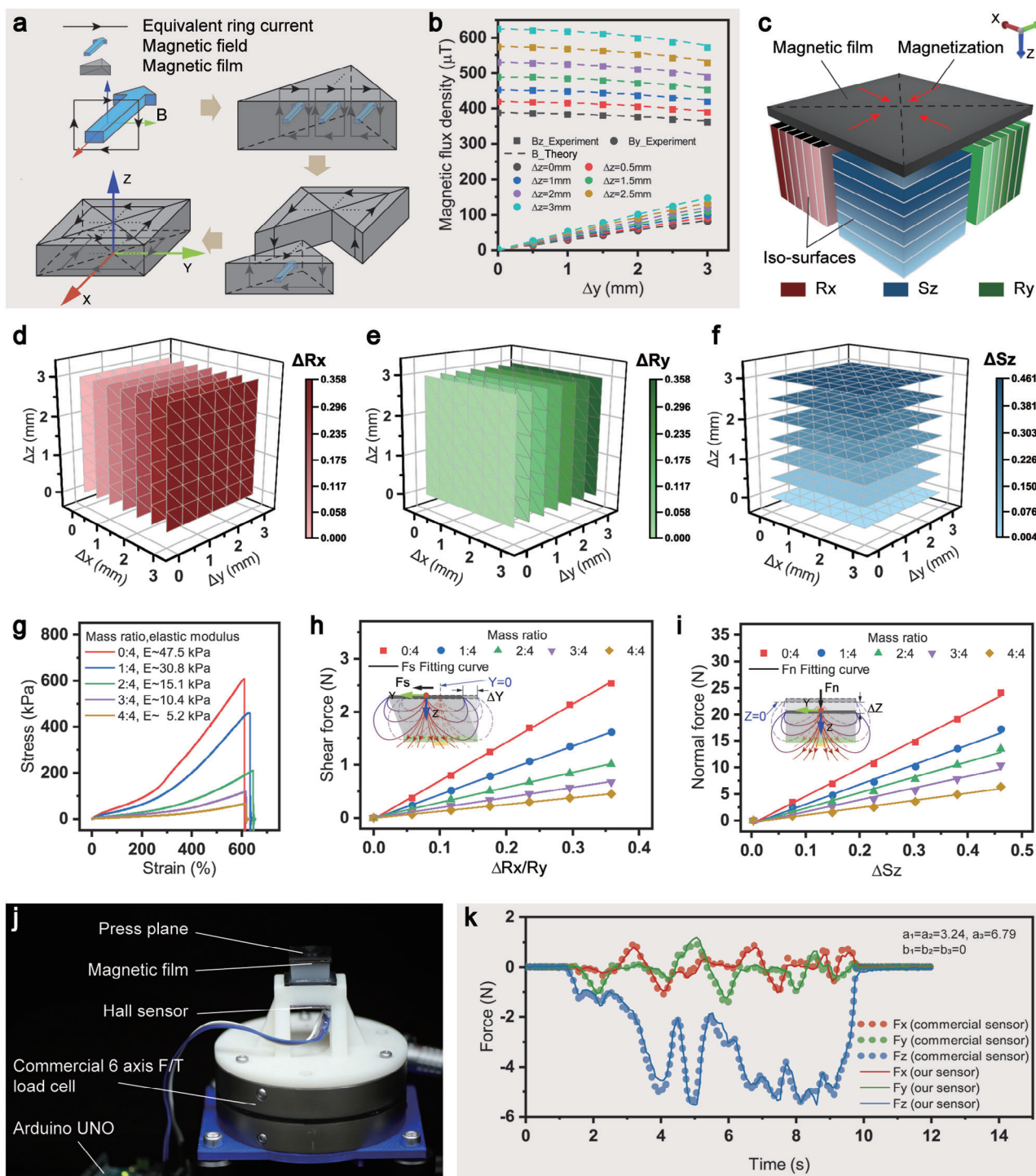


Figure 2. Force decoupling mechanism and calibration of the sensors with substrates with different elastic moduli. a) Schematic diagram of the equivalent of the centripetally magnetized magnetic film's magnetic field as the annular current on the surface of the magnetic film. b) Magnetic distribution under the magnetic film in the y - z plane calculated by the corrected model according to the molecular circulation hypothesis and experimental measurements. c) Distribution of the three decoupling parameters under the magnetic film, where R_x is only related to the X coordinate, S_z is only related to the Z coordinate, and R_y is only related to the Y coordinate. Iso-surfaces represent planes where the decoupling parameters are equal in magnitude. d) Decoupling parameter ΔR_x under the triaxial displacement of the magnetic film. e) Decoupling parameter ΔR_y under the triaxial displacement of the magnetic film. f) Decoupling parameter ΔS_z under the triaxial displacement of the magnetic film. g) Relationships between stress and strain of different silicone elastomers. Accordingly, the relationships between the force and displacement of different "buffer layers" can be calculated. h) Relationships between the shear force output and decoupling parameter ΔR_x (or ΔR_y) of sensors with different buffer layers. i) Relationships between the normal force output and the decoupling parameter ΔS_z of sensors with different buffer layers. j) Experimental device for sensing random forces of human fingers. k) The comparison of the sensing effect for random forces between commercial sensor and our sensor.

the forces in y - and z -directions (Figure 2e,f). In addition, the displacement resolution of the sensor can be obtained here: 0.07 mm in the normal direction and 0.08 mm in the shear direction.

The elastic modulus of the “buffer layer” can be changed to adjust the measurement range and sensitivity of the sensor by mixing silicone oil (PMX-200; viscosity 5 cs) into the silicone. As shown in Figure 2g, when the mass ratio of silicone oil and silicone is gradually increased, the elastic modulus of the soft silicone elastomer gradually decreases. Here, we fabricate five soft silicone elastomers with different mass ratios, whose elastic moduli can be adjusted from 5.2 to 47.5 kPa without a significant change in fracture strain. In this way, our tactile sensor can adapt to different working scenarios, such as measuring large forces with low sensitivity or small forces with high sensitivity. After measuring the force–displacement relationships of the “buffer layers” with different mass ratios (Text S8, Supporting Information), the final calibration curves of the tactile sensors can be obtained and applied to the perception of 3D forces (Figure 2h,i). When the buffer with the minimal elastic modulus (5.2 kPa) is applied, the force resolution of the sensor is 0.137 N in the normal direction and 0.013 N in the shear direction.

After the calibration is completed, we can use the sensor to sense any 3D force. As shown in Figure 2j,k, when the sensor is pressed by human finger at will, our sensor can complete the decoupling perception of arbitrary 3D force like the commercial sensor. See Video S1 (Supporting Information) for more detailed experimental process and data. It should not be ignored that there is a certain gap between the force perceived by our sensor and the commercial sensor at some moments, which is caused by the tilt and twist of the magnetic film in the process of finger pressing, and we have discussed this issue in Text S11 (Supporting Information), respectively.

2.3. Adaptive Grasping and 3D Hybrid Force Sensing

The sensor is mounted on a robotic hand (made by 3D printing, Text S13, Supporting Information) to equip it with the capability of tactile sensing, and the elastic modulus of the soft silicone elastomer can be adjusted to adapt to different working scenarios. As shown in Figure 3a, the robotic hand with a hard-substrate ($E \approx 47.5$ kPa) sensor is prone to damage a fragile object (a tomato), while the robotic hand with a soft-substrate ($E \approx 5.2$ kPa) sensor has difficulty stably grasping a heavy object (an aluminium block). However, after exchanging the substrates, a nondestructive and stable grip is achieved. In addition, it should be emphasized that, through the split-type design and decoupling characteristic, the substrate of the tactile sensor can be easily replaced without moving the Hall sensor and additional calibration. In the process of grasping an object, when the normal force reaches a threshold value, the size of the object can be calculated by reading the rotation angle of the servo (the corresponding relationship between the rotation angle and the size is calibrated in advance). In addition, according to the magnitude of the shear force, the weight of the grasped object can be calculated. In other words, the robotic hand can sense the size and weight of the object simultaneously when grasping an object. Several objects are grasped and measured (Figure 3b); the average size deviation is 0.15 mm, and the average weight deviation is 1.23 g. It should be noted that

since the robotic hand has only one finger mounted with the sensor, the barycenter position of the object affects the weight measurement results.

Using a robot or robotic hand to grasp an object is no longer a novelty, but now, more and more works are showing adaptive grasping (grasping an object that changes in weight or adapting to external disturbances while grasping) as a valuable application.^[46,48–50] Benefiting from the force decoupling function, our tactile sensor can sense normal force and shear force simultaneously, which enables it to conveniently control the friction angle $[\arctan(F_s/F_n)]$ during the grasping process of the robotic hand to achieve adaptive grasping.

The robotic hand equipped with a tactile sensor is used to grasp a volumetric flask (capacity 250 mL, weight 90 g) (Figure 3c) whose weight is changed by continuously filling it with water through a funnel (weight 18 g). Figure 3d shows the curves of F_s , F_n , and F_s/F_n during the experiment. At t_1 (12 s), the robotic hand starts to grasp the volumetric flask and raises the positive pressure to more than 3 N (preset initial normal force). The volumetric flask is released at t_2 (13 s), and the tactile sensor begins to sense the shear force. After maintaining a stable grip until t_3 (17 s), the robotic hand enters the state of adaptive grasping, maintaining F_s/F_n between 0.33 (close to the limit of too tight) and 0.57 (close to the limit of slipping). A funnel is placed at t_4 (21 s), which causes a jitter that is quickly stabilized. With the slow pouring of water (from t_5 , 27 s to t_6 , 50 s), the robotic hand maintains F_s/F_n stably between the two bounds and remains roughly stable even when the weight is rapidly reduced by a researcher lifting the volumetric flask between t_7 (55 s) and t_8 (60 s) (Video S2, Supporting Information). Sensing the magnitude and direction of hybrid forces simultaneously in 3D force space through 3D force decoupling is a unique advantage of our magnetic tactile sensor, which also allows adaptive grasping to cope with inertial forces that arise when grasping vertically and moving horizontally and other 3D interference forces.

The tactile sensor can also be applied in human–machine interactions. We use the magnetic-based tactile sensor as a control “joystick” of a tracked robot, mapping the 3D force applied by the human hand to the different movements of the robot. F_x commands the robot to move forwards and backwards, F_y commands the robot to turn left and right, and F_z commands the robot to grab and place (Figure 3e,f). Through the mapping between force and movement, the robot can complete some simple tasks under control, such as grabbing and transporting objects (Video S3, Supporting Information).

It can be concluded that the split-type magnetic soft tactile sensor can meet the various sensing needs of existing robots and some special human–machine interactions. Moreover, the split-type design allows the sensor to be wirelessly mounted on various robotic hands and shells to act as bionic skin units.

2.4. Specialization of Shear Sensing and Fluid Velocity Measurement

It has been indicated that with the ability of 3D decoupling, the axial offset between Hall sensor and magnetic film during the assembly process will not affect the measurement accuracy of the sensor. It can be regarded as a giant improvement of this work

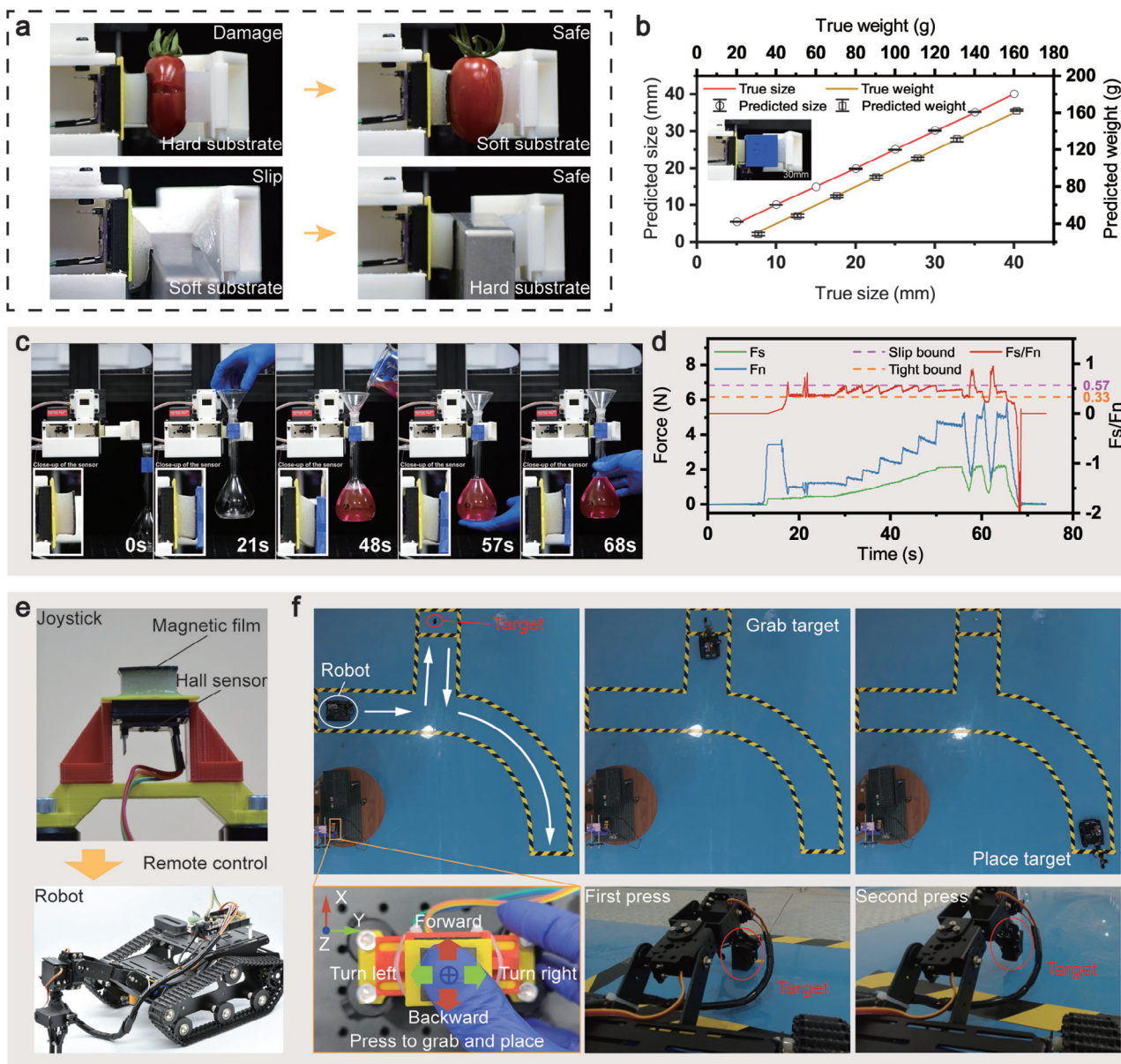


Figure 3. Demonstration of robotic hand force perception, adaptive grasping, and 3D hybrid force sensing. a) Demonstration of gripping different objects by a robotic hand equipped with sensors that have different substrates. This suggests that our sensor can adapt to different work scenarios by changing the substrate. b) Comparison between the sizes and weights predicted by the sensor and the true sizes and weights of the grasped objects. c) Adaptive grasping experiment of the robotic hand grasping a volumetric flask with variable mass and disturbance by external force. d) Curves of the shear force (F_s), the normal force (F_n), and the ratio between them (F_s/F_n) sensed by the sensor during the adaptive grasping experiment. The slip bound and the tight bound represent gripping forces that are too small and too large (F_n), respectively. e) “Joystick” sensor and the tracked robot with a robotic arm. f) Demonstration of using the sensor as a “joystick” to remotely control a tracked robot to grab, transport, and place target.

over previous fitting works and is also an innate guarantee to the split-design of magnetic tactile sensor. Thus, the tactile sensor can also be applied underwater for shear fluid flow velocity sensing, imitating the lateral line of fish, which further illustrates the advantages of split-type sensing and demonstrates the great application potential of the sensor.

The shear force due to the water flow is very small, which can only cause a tiny shear displacement on the solid soft silicone elastomer. Moreover, the adjustment of the elastic modulus of

the soft silicone elastomer by silicone oil is limited, and too much silicone oil prevents the silicone from curing. Consequently, we finally choose to change the structure of the “buffer layer” to observably reduce its shear elastic coefficient and thus achieve the specialization of shear sensing. The fangtooth fish is a deep-sea fish that is the inspiration for the structure of the flow velocity sensor. Living in the deep sea at 1000–5000 m year round, it has no vision and thus develops through evolution a surface tactile sensory organ, the lateral line (Figure 4a), whose slender

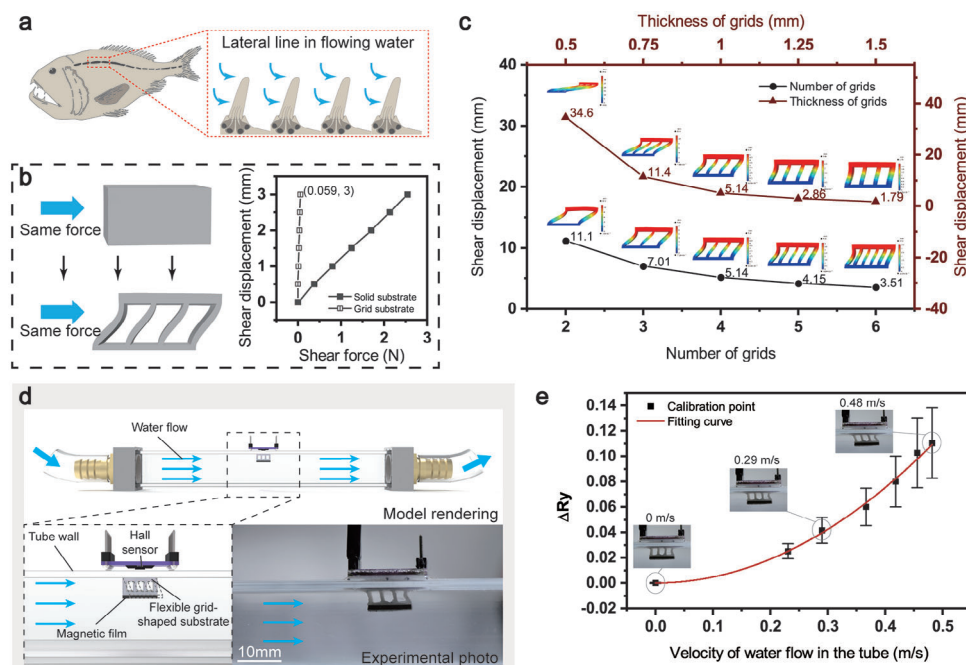


Figure 4. Specialization of shear sensing by biomimetic fish lateral line for flow velocity measurement. a) Illustration of the lateral line structure of the fangtooth fish. b) Left: The grid-shaped substrate design that mimics the lateral line structure. Right: The relationship between the shear displacement and shear force of the two substrates. c) Shear displacement simulation results (in COMSOL) for grids of different structures under the same shear force. d) Diagram of the experimental device for measuring the flow velocity in the tube. Top: Rendering of the device model. Bottom left: Schematic diagram of tactile sensor installation. Bottom right: Experimental photo of flow velocity measurement in the tube. e) Relationship between ΔR_y and the velocity of water flow in the tube.

sensory units enable it to sense changes in the surrounding flow field with great sensitivity, endowing the fangtooth with a superb ability to prey, deal with threats, and identify directions. Mimicking the slender unit array structure of its lateral line and on the premise of maintaining the position and shape of the magnetic film, a grid-shaped “buffer layer” is designed (cured in a grid-type mold). Compared with the solid substrate, the grid-shaped substrate can generate larger shear displacements and magnetic signals under the same shear forces (≈ 38 times), thus exhibiting great sensitivity in the shear direction (Figure 4b).

The shear displacements of grids with different structural parameters under the same shear force (150 N m^{-2}) are simulated and compared in COMSOL Multiphysics (Figure 4c) to determine the appropriate structural parameters of the grid. The forces are applied on the left surfaces of grids to simulate the force of water flow and the bottom surfaces of grids are fixed during simulation. The shear displacement is significantly improved with the reduction in the number and thickness of grids. However, having too few grids bends the magnetic film during deformation, which causes a nonnegligible error. In addition, a grid with too small a thickness is not only fragile and difficult to form but also produces excessive displacement of the magnetic film under the same shear force, which is far beyond the operating range. Therefore, according to the actual flow velocity measurement requirements, we select a substrate with a grid number of 4 and a thickness of 1 mm. The repeated shear displacement experiments of 3600 cycles and the ultimate displacement adaptability test verify that the grid substrate of this structure has sufficient

robustness and stability. See Text S10 (Supporting Information) for details.

A flow velocity measurement experimental device is set up to test and visually demonstrate the wireless measurement of the shear fluid flow velocity through split-type mounting (Figure 4d). The grid-shaped substrate with a magnetic film is a scaled-down version, which is mounted on the inside of the square tube wall, while the Hall sensor is mounted on the outside. The magnetic film is still magnetized in the folding magnetization pattern shown in Figure 1c (below). The center of the centripetally magnetized film and the center of the Hall sensor are aligned by judging the position where the magnetic flux density along the Z-coordinate (B_z) is maximum. The water flow in the square tube is driven by a centrifugal pump, whose power can be controlled to adjust the velocity of water flow in the tube. Moreover, a flowmeter is connected between the pump and the square tube to measure the true velocity of water flow. The experimental photo shows the state of the grid-shaped substrate in the water flow. In addition, since we are only concerned about the sensor's perception of the force in the shear direction, we only need to compare ΔR_y at different flow velocities, which varies most significantly. As shown in Figure 4e, with the increase in the water flow velocity in the square tube, the grid-shaped substrate gradually exhibits increasingly obvious shear deformation, and the ΔR_y also increases. The averages of ΔR_y at various flow velocities are fitted by a quadratic curve with a coefficient of determination over 0.99. However, it can be observed that the value of ΔR_y fluctuates, and the fluctuation increases with increasing flow velocity, which is caused by two main reasons: the first is that the centrifugal pump

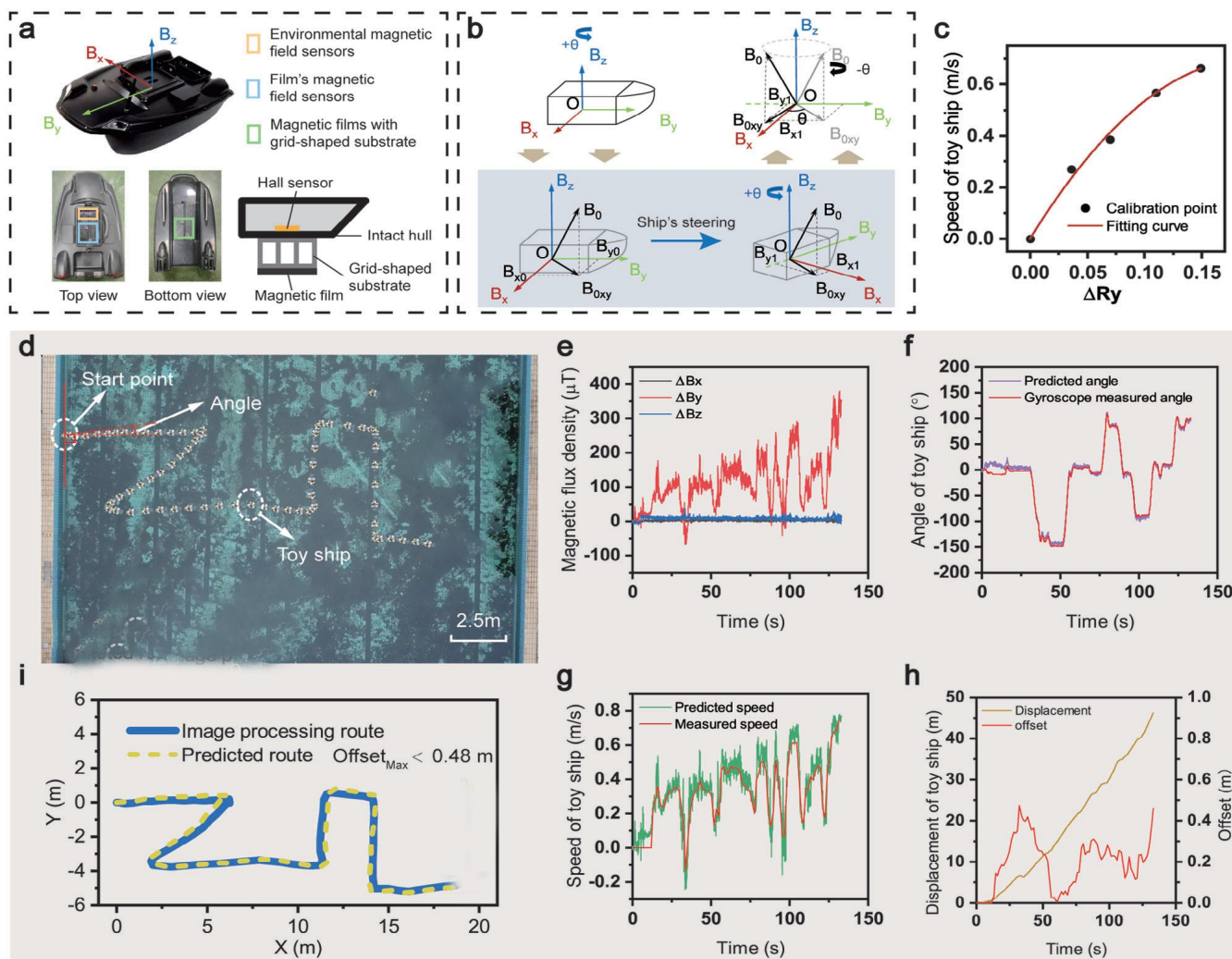


Figure 5. Navigation application of fluid velocity measurement. a) Illustrations of the toy ship and the split-type installation of the soft tactile sensor that is shear-sensing specialized. b) Schematic diagram of the toy ship calculating the steering angle by sensing the constant geomagnetic field in a small range, where we converted the steering angle of the ship into the rotation angle of the geomagnetism in the x - y plane with the sensor as the reference frame. c) Relationship between the speed of the toy ship in the pool and ΔR_y perceived and calculated by the sensor. d) Actual route of the toy ship sailing in the swimming pool. e) Triaxial magnetic field increments of the magnetic film during sailing, which was obtained by subtracting the reading of the environmental magnetic field sensor from the reading of the film's magnetic field sensor. f) Steering angle predicted by the algorithm shown in (b) and the steering angle measured by the gyroscope during sailing. g) Predicted ship speed during sailing and actual ship speed measured by image processing. h) Total sailing displacement of the ship obtained by the speed integral during sailing and the real-time position offset of the whole trajectory obtained by image processing. i) A comparison between the predicted route (obtained by combining the steering angle and the total displacement of the toy ship) and the actual route (obtained by image processing), which had a maximum offset of less than 0.48 m.

causes nonconstant flow velocities, and the more important reason is that unstable vortices are prone to appear near the square grid, which will be addressed by structural optimization of flexible substrates in future research.

2.5. Navigation Application of Fluid Velocity Measurement

Now that the feasibility of measuring the velocity of the fluid in the tube has been verified, in the same way, the velocity of moving objects in water (such as ships, submarines, autonomous underwater vehicles (AUVs), etc.) can also be monitored by measuring

the flow field around them. As shown in **Figure 5a**, two sets of split-type magnetic tactile sensors are installed separately on the inner and outer sides of a toy ship's hull (the data from one of them are selected), achieving concentricity by judging the position where the magnetic flux density along the Z coordinate (B_z) is maximum. The film's magnetic field sensors shown in the blue wireframe are the Hall sensors at the location of the magnetic films, which are used to measure the change in the magnetic flux density caused by the displacement of the magnetic film as well as the movement of the toy ship in the surrounding magnetic field, whose interference can be cancelled by the environmental magnetic field sensors shown in the yellow wireframe. The green

wireframe shows the positions of two magnetic films with grid-shaped substrates. The split-type tactile sensor enables the wireless measurement of the toy ship speed and keeps the hull intact at all times. When the ship moves over a small area (the environmental magnetic field remains constant), the direction of the ship can be directly identified through the 3D magnetic flux density of the geomagnetic field (Figure 5b). B_x – B_y – B_z is the magnetic field coordinate system of the environmental magnetic field sensor. B_0 is the geomagnetic field with a constant direction, B_{0xy} is the projection of the geomagnetic field on the x – y plane, and θ is the steering angle of the ship. When the toy ship rotates θ° , it can be equivalent to the geomagnetic field B_0 rotating θ degrees in the opposite direction in the B_x – B_y – B_z coordinate system. Therefore, θ , the steering angle of the ship, can be obtained according to the angle between B_{0xy} before and after the ship's steering, which can be calculated by

$$\theta = \arccos \left(\frac{B_{x0}B_{x1} + B_{y0}B_{y1}}{\sqrt{B_{x0}^2 + B_{y0}^2} \sqrt{B_{x1}^2 + B_{y1}^2}} \right) \cdot \frac{B_{x0}B_{y1} - B_{x1}B_{y0}}{|B_{x0}B_{y1} - B_{x1}B_{y0}|} \quad (3)$$

where B_{x0} and B_{y0} are the magnetic flux densities along the X and Y coordinates before the ship's steering measured by the sensor, respectively, and B_{x1} and B_{y1} are the magnetic flux densities along the X and Y coordinates after the ship's steering measured by the sensor, respectively.

Figure 5c shows the corresponding ΔRy when the toy ship sails at different speeds in the water, according to which the corresponding relationship between the speed of the toy ship and ΔRy can be obtained by quadratic curve fitting with a coefficient of determination over 0.99.

Combining the steering angle of the toy ship relative to the initial position and the speed along the direction of the ship, we can achieve the path navigation of the toy ship in a small area. The toy ship is remotely controlled to sail in the swimming pool with the route (Figure 5d), and the interval between the positions of every two adjacent toy ship's images is 1.5 s (Video S4, Supporting Information). The magnetic flux density signals (Figure 5e) of the magnetic film after cancelling the interference of the environmental magnetic field are recorded. Moreover, according to the above steering angle algorithm and speed calibration curve, the steering angle of the toy ship relative to the initial position (perpendicular to the pool boundary) and the sailing speed of the toy ship are calculated as shown in Figure 5f,g, where the red curves are the angle measured by the gyroscope and the speed obtained by image processing, respectively. The extremely high coincidence of the curves indicates that the steering angle and the sailing speed predicted by the tactile sensor have satisfactory accuracy. In addition, it can be observed that the angle of the ship is biased to the positive direction at the beginning, so the small deviation in the initial stage is the measurement error of the gyroscope. The relationship between the displacement and time of the toy ship is obtained through the integration of speed to time (Figure 5h). Finally, combining the angle and displacement of the toy ship, we can obtain the predicted route in the x – y displacement plane (Figure 5i), with a maximum offset of less than 0.48 m compared with the actual route. According

to the results, the offset of the predicted route does not exceed 1.03% of the total displacement.

It can be concluded from the above experiment that the tactile sensor has the capability to solely and wirelessly perform the high-precision speed measurement of an object in water while completing navigation in a small area. Even more noteworthy is that since the tactile sensor measures speed relative to the water, it can also be used to perceive and monitor changes and disturbances of the flow field through arrayed and distributed installation. Most of the existing underwater navigation methods are based on the inertial navigation system (INS) because it can provide all the required navigation data independently: acceleration, velocity, position, etc. However, if only the INS is used for navigation, there are inevitable integration errors, which are usually corrected by additional velocity measurement systems. Compared with existing navigation systems and underwater velocity measurement systems, such as the Doppler velocity log (DVL) system,^[51] computer vision systems,^[52] and pressure sensing systems,^[2,53] our tactile sensor can measure velocity wirelessly, keeping the hull or bulkhead intact, with a small volume, light weight, flexibility, and low cost, which demonstrates the potential on the velocity measurement of the underwater vehicles, especially deep-sea small AUVs.

3. Conclusion

The sensor proposed in this paper is a sandwich-like magnetic soft tactile sensor with a specially magnetized film, which enables simple and intuitive 3D force decoupling perception through magnetic energy. Here, we illustrated the biomimetic layered structure of the magnetic soft tactile sensor and succinctly demonstrated its basic 3D force decoupling function as well as its good frequency adaptability and repeatability. Experimental measurements and modelling calculations showed that the three decoupling parameters (R_x , R_y , and S_z) we proposed could achieve the decoupling of triaxial displacements below the centripetally magnetized thin film, which enabled the decoupling of triaxial forces. Moreover, these replaceable “buffer layers” with different elastic moduli contributed to the adjustable force measurement ranges and sensitivities of the sensor. The grasping experiments of the robotic hand indicated that the magnetic-based soft tactile sensor had excellent accuracy and stability, and the task of 3D hybrid force sensing further verified the feasibility of 3D force decoupling. Based on the proposed method and imitating the lateral line of fish, we designed and fabricated an optimized “buffer layer” that could generate ≈ 38 times the shear displacement under the minimal thrust of water flow compared to a solid layer. Consequently, the lateral-line-like tactile sensor could sense and measure the speed of water flow. Moreover, benefiting from the wireless characteristic of magnetic field sensing, the split-type tactile sensor could maintain the integrity of the installation position during operation without losing airtightness and strength (adapted to the deep-sea working environment). The sensor was installed on the bottom of a toy ship as the “lateral line” to measure the speed of the ship, proving the feasibility of low-cost area navigation and environmental perception.

In summary, compared with traditional tactile sensors, our sensor has two unique capabilities. One is the split-type design and wireless sensing, which can not only improve the

flexibility and physical robustness of the sensor but also make it more convenient to replace the flexible part to adjust the measurement range and sensitivity when needed. More importantly, these characteristics make our sensor capable of some sensing tasks in extreme environments that ordinary sensors are not capable of. The second is the 3D hybrid force decoupling, which adds one force perception dimension to our sensor, enabling it to have a static force perception capability that is closer and more similar to that of human skin, just through its extremely simple structure and low cost. These two capabilities undoubtedly expand the applications of magnetic-based tactile sensors. Our sensor also provides solutions to some major problems in other fields, such as flexible electronics, bionic robots, and human-machine interactions.

However, considering functional expansion and future applications, there are still many further improvements that can be made for this sensor and its applications. First, the magnetic film of our sensor must be kept straight during operation, but the magnetic film rotates and sags in practical applications, which can be solved by in-depth research on the magnetic field model of the magnetic film and machine learning. Second, to facilitate demonstration and explain that the magnetic sensor has a large wireless distance, the sensor has a large size, which can be reduced to meet application requirements. Third, this paper focused on the sensor unit, but the array and distributed design can greatly expand the functions and applications of the sensor. Fourth, the sensor is susceptible to interference from external magnetic fields. The Halbach magnetization in Yan's work^[46] and the gradiometric magnetic force sensor in Le Signor's work^[47] have inspired us, and based on these studies, we hope to solve this problem and optimize our sensor in future work. Besides, although the 3D decoupling theory eliminates the influence of the magnetic film installation position on the repeatability of the sensor, there are still several external factors that may cause the repeatability issue: the uniformity of the magnetic thin film, i.e., the mixture of micromagnets and silicone polymer, the size distribution of micromagnets, the magnetic properties of micromagnets between different batches; stiffness difference of the buffer layers between different batches; and the sensor to sensor differences in the Hall sensors. However, in our practical experiment, mixing by the planetary mixer and molding by the 3D printed mold are enough to ensure our sensors' sufficient repeatability. In conclusion, this paper reports a split-type magnetic soft tactile sensor with a 3D force decoupling function, which is more similar to human skin in terms of flexibility and perception and has a strong application ability for underwater environment perception. In the future, the applications of this sensor can be expanded by miniaturization, arraying or enlarging, and this sensor has promising applications in other fields, such as flexible electronics, bionic robots, and human-machine interactions.

4. Experimental Section

Preparation and Magnetization of the Magnetic Film: The magnetic material of the film was a mixture of SE 1700 base (DOWSIL, 11.71 wt%), SE 1700 catalyst (DOWSIL, 1.17 wt%), Ecoflex 00-30 Part B (Shanghai Zhixin Corp, 21.78 wt%), fumed silica nanoparticles (Aladdin Biochemistry Technology Corp, 2.72 wt%), and NdFeB microparticles (Jianghuai Ciye Corp,

62.62 wt%).^[40] The components were mixed at 2000 rpm for 3 min, followed by defoaming at 2000 rpm for 2 min. The thoroughly mixed magnetic paste was placed between two release plates, which were squeezed to a distance of 1 mm. Then, they were put together in an oven at 120 °C for 1.5 h to fully cure the magnetic material, after which the magnetic film was cut to a size of 20 × 20 mm and folded into the shape of an arrowhead through a cross-shaped holder. Finally, it was magnetized in a uniform magnetic field (4.0 T) generated by a pulse coil (JH12160).

Fabrication of the Buffer Layer Elastomer: The buffer layer elastomer between the magnetic film and the Hall sensor is Ecoflex 00-30 mixed with silicone oil (PMX-200; viscosity 5 cs). The Ecoflex 00-30 components Part A and Part B and silicone oil were mixed at 2000 rpm for 1 min, followed by defoaming at 2000 rpm for 2 min. Then, they were injected into a mold (fabricated by 3D printing) with a size of 20 × 20 × 10 mm to cure naturally at room temperature. The grid-shaped substrates were fabricated in a grid-shaped mold in the same way, see Text S12 (Supporting Information) for more details.

Assembly of the Magnetic Soft Tactile Sensor: The assembly between each layer of the sensor mainly used silicone soft glue (DL-1020) for bonding. After the silicon elastomer was fully cured, the mold base was removed, and the rest was inverted. The elastomer was then evenly coated with glue (DL-1020, 0.2–0.3 mL, evenly coat the contact surface), covered with the magnetic film, and pressed flat with the 3D-printed mold base. The glue was completely cured at room temperature for 24 h. After the combination of the flexible layer was completed, the target partition was evenly coated with glue to bond the flexible layer. The Hall sensor used to measure the magnetic field of the film was MLX90393, which was also bonded to the other side of the target partition. Before the glue of the sensor cured, the center of the magnetic film and the Hall sensor was aligned by judging the position where the magnetic flux density along the Z coordinate (B_z) was maximum. In fact, since the decoupled model determines the position offset of the magnetic film by measuring the changes of R_x , R_y , and S_z , complete alignment of the magnetic film is not necessary. In application scenarios where asymmetric operating ranges are required, offset installation can be performed, see Text S12 (Supporting Information) for more details.

Calibration of the Buffer Layer: The magnetic soft tactile sensor was mounted on a fixed aluminium plate, and the dynamometer (Zhiqu, DS2-5N and 100N) was fixed to a 3D motion platform (PMS-3) by a 3D-printed fixture. The dynamometer was driven by the motion platform and pressed the magnetic film to produce shear and normal displacements with a step size of 0.5 mm, and during the process, the readings of dynamometer were recorded.

Supporting Information

Supporting Information is available from the Wiley Online Library or from the author.

Acknowledgements

Conflict of Interest

The authors declare no conflict of interest.

Data Availability Statement

The data that support the findings of this study are available from the corresponding author upon reasonable request.

Keywords

3D force decoupling, artificial e-skin, flexible electronics, magnetic, tactile sensors

Received: September 30, 2023

Revised: November 15, 2023

Published online: December 7, 2023

- [1] M. Krieg, K. Nelson, K. Mohseni, *Nat. Mach. Intell.* **2019**, 1, 216.
- [2] W. Wang, Y. Li, X. Zhang, C. Wang, S. Chen, G. Xie, *2016 IEEE Int. Conf. on Robotics and Automation (ICRA)*, IEEE, Stockholm, Sweden, **2016**, pp. 4737.
- [3] Q. He, Y. Wu, Z. Feng, C. Sun, W. Fan, Z. Zhou, K. Meng, E. Fan, J. Yang, *Nano Energy* **2019**, 59, 689.
- [4] S. Chun, J.-S. Kim, Y. Yoo, Y. Choi, S. J. Jung, D. Jang, G. Lee, K.-I. Song, K. S. Nam, I. Youn, D. Son, C. Pang, Y. Jeong, H. Jung, Y.-J. Kim, B.-D. Choi, J. Kim, S.-P. Kim, W. Park, S. Park, *Nat. Electron.* **2021**, 4, 429.
- [5] H. Guo, Y. J. Tan, G. Chen, Z. Wang, G. J. Susanto, H. H. See, Z. Yang, Z. W. Lim, L. Yang, B. C. K. Tee, *Nat. Commun.* **2020**, 11, 5747.
- [6] P. Li, L. Xie, M. Su, P. Wang, W. Yuan, C. Dong, J. Yang, *Nano Energy* **2022**, 101, 107571.
- [7] G. Li, S. Liu, L. Wang, R. Zhu, *Sci. Robot.* **2020**, 5, eabc8131.
- [8] X. Liao, W. Wang, L. Wang, H. Jin, L. Shu, X. Xu, Y. Zheng, *Nano Energy* **2021**, 80.
- [9] S. Jung, J. H. Kim, J. Kim, S. Choi, J. Lee, I. Park, T. Hyeon, D.-H. Kim, *Adv. Mater.* **2014**, 26, 4825.
- [10] S. Lim, D. Son, J. Kim, Y. B. Lee, J.-K. Song, S. Choi, D. J. Lee, J. H. Kim, M. Lee, T. Hyeon, D.-H. Kim, *Adv. Funct. Mater.* **2015**, 25, 375.
- [11] Y. Jiang, Z. Liu, N. Matsuhisa, D. Qi, W. R. Leow, H. Yang, J. Yu, G. Chen, Y. Liu, C. Wan, Z. Liu, X. Chen, *Adv. Mater.* **2018**, 30, 1706589.
- [12] S. Zhang, A. Chhetry, M. A. Zahed, S. Sharma, C. Park, S. Yoon, J. Y. Park, *npj Flexible Electron.* **2022**, 6, 11.
- [13] B. C.-K. Tee, A. Chortos, A. Berndt, A. K. Nguyen, A. Tom, A. McGuire, Z. C. Lin, K. Tien, W.-G. Bae, H. Wang, P. Mei, H.-H. Chou, B. Cui, K. Deisseroth, T. N. Ng, Z. Bao, *Science* **2015**, 350, 313.
- [14] Y. Wu, Y. Liu, Y. Zhou, Q. Man, C. Hu, W. Asghar, F. Li, Z. Yu, J. Shang, G. Liu, M. Liao, R. Li, *Sci. Robot.* **2018**, 3, eaat0429.
- [15] C. Dagdeviren, Y. Su, P. Joe, R. Yona, Y. Liu, Y. Kim, Y. Huang, A. R. Damadoran, J. Xia, L. W. Martin, Y. Huang, J. A. Rogers, *Nat. Commun.* **2014**, 5, 4496.
- [16] J. Wang, J. Jiang, C. Zhang, M. Sun, S. Han, R. Zhang, N. Liang, D. Sun, H. Liu, *Nano Energy* **2020**, 76, 105050.
- [17] Y. Kim, J. Song, S. Hong, S. Ahn, *npj Flexible Electron.* **2022**, 6, 52.
- [18] J. Park, Y. Lee, J. Hong, M. Ha, Y.-D. Jung, H. Lim, S. Y. Kim, H. Ko, *ACS Nano* **2014**, 8, 4689.
- [19] Y. Wang, H. Wu, L. Xu, H. Zhang, Y. Yang, Z. L. Wang, *Sci. Adv.* **2020**, 6, eabb9083.
- [20] C.-L. Choong, M.-B. Shim, B.-S. Lee, S. Jeon, D.-S. Ko, T.-H. Kang, J. Bae, S. H. Lee, K.-E. Byun, J. Im, Y. J. Jeong, C. E. Park, J.-J. Park, U.-I. Chung, *Adv. Mater.* **2014**, 26, 3451.
- [21] Y. Luo, Y. Li, P. Sharma, W. Shou, K. Wu, M. Foshey, B. Li, T. Palacios, A. Torralba, W. Matusik, *Nat. Electron.* **2021**, 4, 314.
- [22] Q. Su, Q. Zou, Y. Li, Y. Chen, S. Teng, J. T. Kelleher, R. Nith, P. Cheng, N. Li, W. Liu, S. Dai, Y. Liu, A. Mazursky, J. Xu, L. Jin, P. Lopes, S. Wang, *Sci. Adv.* **2021**, 7, eabi4563.
- [23] A. Frutiger, J. T. Muth, D. M. Vogt, Y. Menguec, A. Campo, A. D. Valentine, C. J. Walsh, J. A. Lewis, *Adv. Mater.* **2015**, 27, 2440.
- [24] Y. Zang, F. Zhang, D. Huang, X. Gao, C. Di, D. Zhu, *Nat. Commun.* **2015**, 6, 6269.
- [25] N. Bai, L. Wang, Q. Wang, J. Deng, Y. Wang, P. Lu, J. Huang, G. Li, Y. Zhang, J. Yang, K. Xie, X. Zhao, C. F. Guo, *Nat. Commun.* **2020**, 11, 209.
- [26] A. Yamaguchi, C. G. Atkeson, *IEEE-RAS 16th Int. Conf. Humanoid Robots (Humanoids)*, IEEE, Cancun, Mexico, **2016**, pp. 1045.
- [27] W. Yuan, S. Dong, E. H. Adelson, *Sensors* **2017**, 17, 2762.
- [28] B. Ward-Cherrier, N. Pestell, L. Cramphorn, B. Winstone, M. E. Giannaccini, J. Rossiter, N. F. Lepora, *Soft Robot.* **2018**, 5, 216.
- [29] Z. Song, J. Yin, Z. Wang, C. Lu, Z. Yang, Z. Zhao, Z. Lin, J. Wang, C. Wu, J. Cheng, Y. Dai, Y. Zi, S. Huang, X. Chen, J. Song, G. Li, W. Ding, *Nano Energy* **2022**, 93, 106798.
- [30] P. Maharjan, T. Bhatta, M. Salauddin, M. S. Rasel, M. T. Rahman, S. M. S. Rana, J. Y. Park, *Nano Energy* **2020**, 76, 105071.
- [31] X. Qu, Z. Liu, P. Tan, C. Wang, Y. Liu, H. Feng, D. Luo, Z. Li, Z. L. Wang, *Sci. Adv.* **2022**, 8, eabq2521.
- [32] K. Park, H. Yuk, M. Yang, J. Cho, H. Lee, J. Kim, *Sci. Robot.* **2022**, 7, eabm7187.
- [33] J. Park, M. Kim, Y. Lee, H. S. Lee, H. Ko, *Sci. Adv.* **2015**, 1, e1500661.
- [34] Y. Pang, X. Xu, S. Chen, Y. Fang, X. Shi, Y. Deng, Z. Wang, C. Cao, *Nano Energy* **2022**, 96, 107137.
- [35] T. P. Tomo, M. Regoli, A. Schmitz, L. Natale, H. Kristanto, S. Somlor, L. Jamone, G. Metta, S. Sugano, *IEEE Robot. Autom. Lett.* **2018**, 3, 2584.
- [36] H. Wang, G. de Boer, J. Kow, A. Alazmani, M. Ghajari, R. Hewson, P. Culmer, *Sensors* **2016**, 16, 1356.
- [37] C. Ledermann, S. Wirges, D. Oertel, M. Mende, H. Woern, *2013 IEEE 17th Int. Conf. on Intelligent Engineering Systems (INES)*, IEEE, San Jose, Costa Rica, **2013**, pp. 55.
- [38] A. C. Holgado, J. A. A. Lopez, A. Schmitz, T. P. Tomo, S. Somlor, L. Jamone, S. Sugano, *IEEE/RSJ Int. Conf. Intelligent Robots Systems (IROS)*, IEEE, Madrid, Spain, **2018**, pp. 2582.
- [39] P. Ribeiro, M. A. Khan, A. Alfadhel, J. Kosel, F. Franco, S. Cardoso, A. Bernardino, A. Schmitz, J. Santos-Victor, L. Jamone, *IEEE Robot. Autom. Lett.* **2017**, 2, 971.
- [40] J. Man, G. Chen, J. Chen, *Biosensors* **2022**, 12, 1054.
- [41] H. Hu, C. Zhang, C. Pan, H. Dai, H. Sun, Y. Pan, X. Lai, C. Lyu, D. Tang, J. Fu, P. Zhao, *ACS Nano* **2022**, 16, 19271.
- [42] Y. Zhou, X. Zhao, J. Xu, Y. Fang, G. Chen, Y. Song, S. Li, J. Chen, *Nat. Mater.* **2021**, 20, 1670.
- [43] T. Kawasetsu, T. Horii, H. Ishihara, M. Asada, *Sensors* **2018**, 18, 587.
- [44] D. Tang, C. Zhang, H. Sun, H. Dai, J. Xie, J. Fu, P. Zhao, *Nano Energy* **2021**, 89, 106424.
- [45] Y. Kim, H. Yuk, R. Zhao, S. A. Chester, X. Zhao, *Nature* **2018**, 558, 274.
- [46] Y. Yan, Z. Hu, Z. Yang, W. Yuan, C. Song, J. Pan, Y. Shen, *Sci. Robot.* **2021**, 6, eabc8801.
- [47] T. Le Signor, N. Dupre, G. F. Close, *IEEE Robot. Autom. Lett.* **2022**, 7, 3070.
- [48] J. Yan, H. Zheng, F. Sun, H. Liu, Y. Song, B. Fang, *IEEE Robot. Autom. Lett.* **2022**, 7, 12371.
- [49] Y. Zhang, J. Yang, X. Hou, G. Li, L. Wang, N. Bai, M. Cai, L. Zhao, Y. Wang, J. Zhang, K. Chen, X. Wu, C. Yang, Y. Dai, Z. Zhang, C. F. Guo, *Nat. Commun.* **2022**, 13, 1317.
- [50] S.-J. Huang, W.-H. Chang, J.-Y. Su, *Int. J. Control Autom.* **2017**, 15, 2272.
- [51] P. Liu, B. Wang, Z. Deng, M. Fu, *IEEE Sens. J.* **2018**, 18, 2994.
- [52] A. Manzanilla, S. Reyes, M. Garcia, D. Mercado, R. Lozano, *IEEE Robot. Autom. Lett.* **2019**, 4, 1351.
- [53] W. A. Ramirez, Z. Q. Leong, H. D. Nguyen, S. G. Jayasinghe, *Ocean Eng.* **2020**, 213, 107771.